AutoTAB: Automatic Tracking Algorithm for Bipolar Magnetic Regions

Anu Sreedevi,[1] Bibhuti Kumar Jha,[2,3] Bidya Binay Karak,[1] and Dipankar Banerjee[3,4,5]

[1]*Department of Physics, Indian Institute of Technology (Banaras Hindu University), Varanasi 221005, India*
[2]*Southwest Research Institute, Boulder, CO 80302, USA*
[3]*Aryabhatta Research Institute of Observational Sciences, Nainital 263002, Uttarakhand, India*
[4]*Indian Institute of Astrophysics, Koramangala, Bangalore 560034, India*
[5]*Center of Excellence in Space Sciences India, IISER Kolkata, Mohanpur 741246, West Bengal, India*

ABSTRACT

Bipolar Magnetic Regions (BMRs) provide crucial information about solar magnetism. They exhibit varying morphology and magnetic properties throughout their lifetime, and studying these properties can provide valuable insights into the workings of the solar dynamo. The majority of previous studies have counted every detected BMR as a new one and have not been able to study the full life history of each BMRs. To address this issue, we have developed an Automatic Tracking Algorithm (AutoTAB) for BMRs, that tracks the BMRs for their entire lifetime or throughout their disk passage. AutoTAB uses the binary maps of detected BMRs to automatically track the regions. This is done by differentially rotating the binary maps of the detected regions and checking for overlaps between them. In this first article of this project, we provide a detailed description of the working of the algorithm and evaluate its strengths and weaknesses. We also compare its performance with other existing tracking techniques. AutoTAB excels in tracking even for the small features and it successfully tracks 9152 BMRs over the last two solar cycles (1996–2020), providing a comprehensive dataset that depicts the evolution of various properties for each tracked region. The tracked BMRs follow familiar properties of solar cycles except for these small BMRs that appear at all phases of the solar cycle and show weak latitudinal dependency, which is represented through the butterfly diagram. Finally, we discuss the possibility of adapting our algorithm to other datasets and expanding the technique to track other solar features in the future.

Keywords: Bipolar sunspot groups(156) — Solar magnetic fields(1503) — Solar activity(1475)

1. INTRODUCTION

Bipolar Magnetic Regions (BMRs) remain one of the most predominant signatures of solar magnetism as observed on the surface of the Sun. The number of such regions at a given time represents the solar activity that waxes and wanes cyclically over a period of 11 years (Schwabe 1844; Hathaway 2015). These BMRs are generally the source regions of solar eruptive events (Schrijver 2009), and hence they are crucial for the understanding of space weather conditions. BMRs are observed to be tilted by an angle with respect to the equa-

tor, which is found to increase statistically with latitude, which is known as Joy's law (Hale et al. 1919). It is observed that the decay and dispersal of tilted BMRs produce the poloidal field in the Sun through Babcock-Leighton mechanism (Babcock 1961; Leighton 1964; Mordvinov et al. 2022).

Sunspot groups which mimic the locations of BMRs, have been traditionally used for the study of BMR properties (e.g., Howard 1991, 1996; Sivaraman et al. 2007; Dasi-Espuig et al. 2010) because of the unavailability of magnetogram data. Since the early 1970s, regular full-disk measurements of the Sun's magnetic field have been started, and now there exist vast archived data of solar magnetograms from the different ground-based (Synoptic Optical Long-term Investigations of the Sun (SOLIS; Keller et al. 2003), Global Oscillation Network

anubsreedevi.rs.phy20@itbhu.ac.in

karak.phy@iitbhu.ac.in

Group (GONG; Harvey et al. 1996)) and space-based (Michelson Doppler Image (MDI; Scherrer et al. 1995) and Helioseismic and Magnetic Imager (HMI; Schou et al. 2012)) observatories. To exploit such a large volume of data for the understanding of BMRs and solar magnetism, various automatic methods has been developed (Stenflo & Kosovichev 2012; Tlatov & Pevtsov 2014; Jha et al. 2020). In all these studies, each detection of BMRs has been treated as a new one (Stenflo & Kosovichev 2012; Jha et al. 2020). However, this approach may influence the analysis as bigger BMRs have a longer lifetime and thereby will have higher weightage in the analysis (van Driel-Gesztelyi & Green 2015). Furthermore, BMR properties, including its morphology, magnetic field strength, and tilt angle, evolve significantly over its lifetime (Ugarte-Urra et al. 2015; Getling & Buchnev 2019; Schunker et al. 2019, 2020). Hence, to overcome these limitations, it is essential to track the BMR to get insight into the physics of the formation and evolution of BMR. Moreover, the automatic detection and tracking of magnetic regions also become essential for monitoring solar activity and events (McAteer et al. 2005; LaBonte et al. 2007). Therefore, an enormous effort has been made to develop automatic algorithms to track the BMRs (Higgins et al. 2011; Muñoz-Jaramillo et al. 2016).

Solar Monitor Active Region Tracking (SMART; Higgins et al. 2011) was developed for the automatic detection and tracking of magnetic active regions in real-time for solar eruptive event prediction. Although SMART does a decent job in identifying and extracting various magnetic features, it tends to miss some quiet Sun magnetic regions. The Bipolar Active Region Detection (BARD; Muñoz-Jaramillo et al. 2016) is an another algorithm developed for the detection and tracking of BMRs. It uses similar techniques to detect BMRs as SMART but uses the dual-maximum flux-weighted overlap method for feature association. The BARD uses human supervision to correct any errors in detection and tracking. Furthermore, space-Weather MDI Active Region Patches (SMARP; Bobra et al. 2021) and Space-Weather HMI Active Region Patches (SHARP; Bobra et al. 2014) are the data sets derived from MDI and HMI magnetograms, respectively which provide the tracked maps of active regions identified in the magnetic image of the Sun. We note that in SMARP and SHARP, active regions are not necessarily the BMRs, where a decent flux balance condition holds.

To the best of our knowledge, there is no existing catalog that can provide the properties of the individual BMRs throughout their lifetime or at least the course of their lifetimes. Therefore, we overcome the limita-

tion of existing BMR tracking algorithms and develop a completely automatic method to track the BMR, which can be implemented in all sets of magnetogram data. In Section 2, we have presented a detailed description of our tracking algorithm and its comparison with the existing one. In Section 3, we presented some representative results based on our tracking algorithm, and finally, in Section 4, we conclude with our insight on this new algorithm.

2. DATA AND METHOD

In our study, we use the Line-of-Sight (LOS) magnetograms (Cycles 23 and 24) for the period of September 1996 to December 2019 from Michelson Doppler Imager (MDI: 1996–2011; Scherrer et al. 1995) and Helioseismic and Magnetic Imager (HMI: 2010–present; Schou et al. 2012) onboard the Solar and Heliospheric Observatory(SOHO) and Solar Dynamic Observatory (SDO) spacecraft, respectively. Here, we utilize all the magnetograms from MDI, which comes with a cadence of 96 minutes in 1024×1024 resolution with a pixel size of $2'' \times 2''$ (spatial resolution of $4'' \times 4''$). Although HMI provides magnetogram data with the cadence of 45 sec in 4096×4096 resolution with the pixel size of $0.5'' \times 0.5''$ (spatial resolution of $1'' \times 1''$), for the ease of computation, we use one image every 96 minutes as available for MDI.

The data sets used for the mentioned period contain 1,26,381 fits images (MDI: 56,384 HMI: 69,997). The number of defective pixels (identified as "Not a Number") on the solar disk is calculated for every magnetogram. If the number is found to be greater than 100, the magnetogram is considered defective and not included in the analysis.

The data in the magnetograms corresponds to the line-of-sight (LOS) component of the surface magnetic field, which is integrated across a spatial resolution kernel. Hence, they suffer from the projection effect, which is inversely proportional to the cosine of heliocentric angular distance[1]. We correct the LOS component for this effect by assuming the magnetic field is normal to the solar surface and initially restrict ourselves to less than 0.9 $R_\odot$. Furthermore, we also noticed that as we go close to the limb, multiple closely lying BMRs are identified as one by the detection (Jha et al. 2020). As this may significantly affect the tracking, we later restrict our analysis only between $\pm45°$ of longitudes.

2.1. BMR Detection Algorithm

---

[1] Angular Distance of the pixel from the disk center.

Algorithm developed to detect BMRs from the LOS magnetograms follows the prescription given in Stenflo & Kosovichev (2012), which was also used in Jha et al. (2020) with slight modifications. A brief description of the detection algorithm is as follows. In the first step, the LOS magnetograms are corrected for projection effects to obtain the magnetic field component normal to the solar surface. After that, an appropriate threshold is used for every magnetogram based on its average magnetic field value to isolate the strong magnetic field regions. This step is followed by a moderate flux balance condition (Stenflo & Kosovichev 2012) to get the BMRs. The identified BMRs are shown in Figure 1a. In the case of HMI magnetograms, we re-binned the magnetogram from 4096×4096 pixels to 1024×1024 pixels to further reduce the computational time. By comparing the detected BMRs from the original and the binned data, we find that this binning does not affect the detection of BMRs. These identified regions from both data sets are stored in the form of a binary mask, which acts as the starting point of our tracking algorithm.
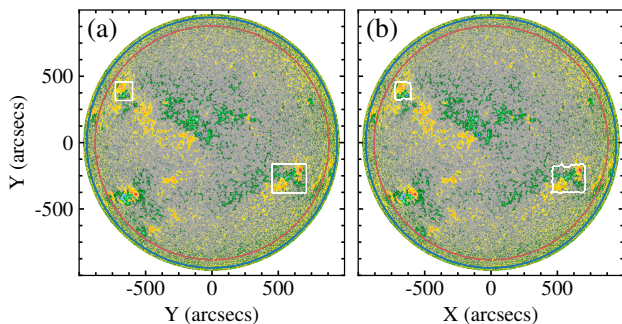

Figure 1: (a) Magnetogram for 15-11-2000 20:48 with the detected BMRs represented by white rectangular boxes. (b) Same as (a) but after the pre-processing (described in Section 2.2) of BMR masks. The solid blue and red dashed circle represents 1.0 $R_\odot$ and 0.9 $R_\odot$, respectively.

2.2. Pre-processing of BMR Masks

In Jha et al. (2020), the identified BMR regions masks are stored as the rectangular regions around the BMRs (see Figure 1a), which include additional pixels which are not part of BMR regions and may affect the tracking, particularly in the case of closely spaced BMRs during high activity period. Hence, to get rid of those extra pixels before we start the tracking, we go through the the following pre-processing steps.

To get the exact morphology of the BMR in the rectangular regions of interest (ROI), we picked all the pixels with magnetic fields greater than 100 G. This threshold

not only leads to a few fragmented pixels in ROI but also separate poles of the BMR, as they do not always touch each other's boundaries. To eliminate the fragmented pixels, as well as to join the separated poles, we apply the morphological closing operation[2] using a circular kernel with an initial radius of six pixels followed by an area threshold of 50 pixels. The radius of the kernel is systematically increased up to 9 pixels at the step of one pixel until the number of connected regions matches with the number of identified BMRs (i.e., the number of rectangular regions, see Figure 1a) in that magnetogram. Finally, the flux balance condition (Stenflo & Kosovichev 2012; Jha et al. 2020) is verified for each region to ensure that they are BMRs.

In Figure 1b, white contours represent the BMRs after the pre-processing steps. The information of detected BMRs after pre-processing is also stored as binary masks so that it can be used for tracking.

2.3. BMR Tracking Algorithm

Now we come to the core of the work, and that is to develop an automatic algorithm to track all of the identified BMRs. Our tracking algorithm employs binary masks obtained from the last step of pre-processing to follow the interested regions over their lifetime/disk passage. The idea of the BMR tracking algorithm comes from the sunspot tracking algorithm developed in Jha et al. (2021), which is modified considerably to track the BMRs in the magnetograms. Now, we discuss the steps of our tracking algorithm as follows.

1. At the first step, a binary mask is selected from the archive (Figure 2a1). A BMR, which is not tracked already (see the marked circle in Figure 2a1), is isolated in a separate binary mask (Figure 2b1), and a unique BMR-ID (say 10001) is assigned to it.

2. Now, we calculate the maximum tracking period (T_{max}) i.e., the time it takes to reach the west limb, based on the heliographic latitude θ_{BMR} and longitude ϕ_{BMR} of the BMR as,

$$T_{max} = \frac{90° - \phi_{BMR}}{\Omega(\theta_{BMR})}. \qquad (1)$$

Here, $\Omega(\theta_{BMR})$ is the photospheric differential rotation rate (Jha et al. 2021) for given θ_{BMR}.

3. In the next step, we take a sequence of observations (binary masks; say Sequence-a, as shown in Figure 2a1 – a4) falling in the range of T_{max}.

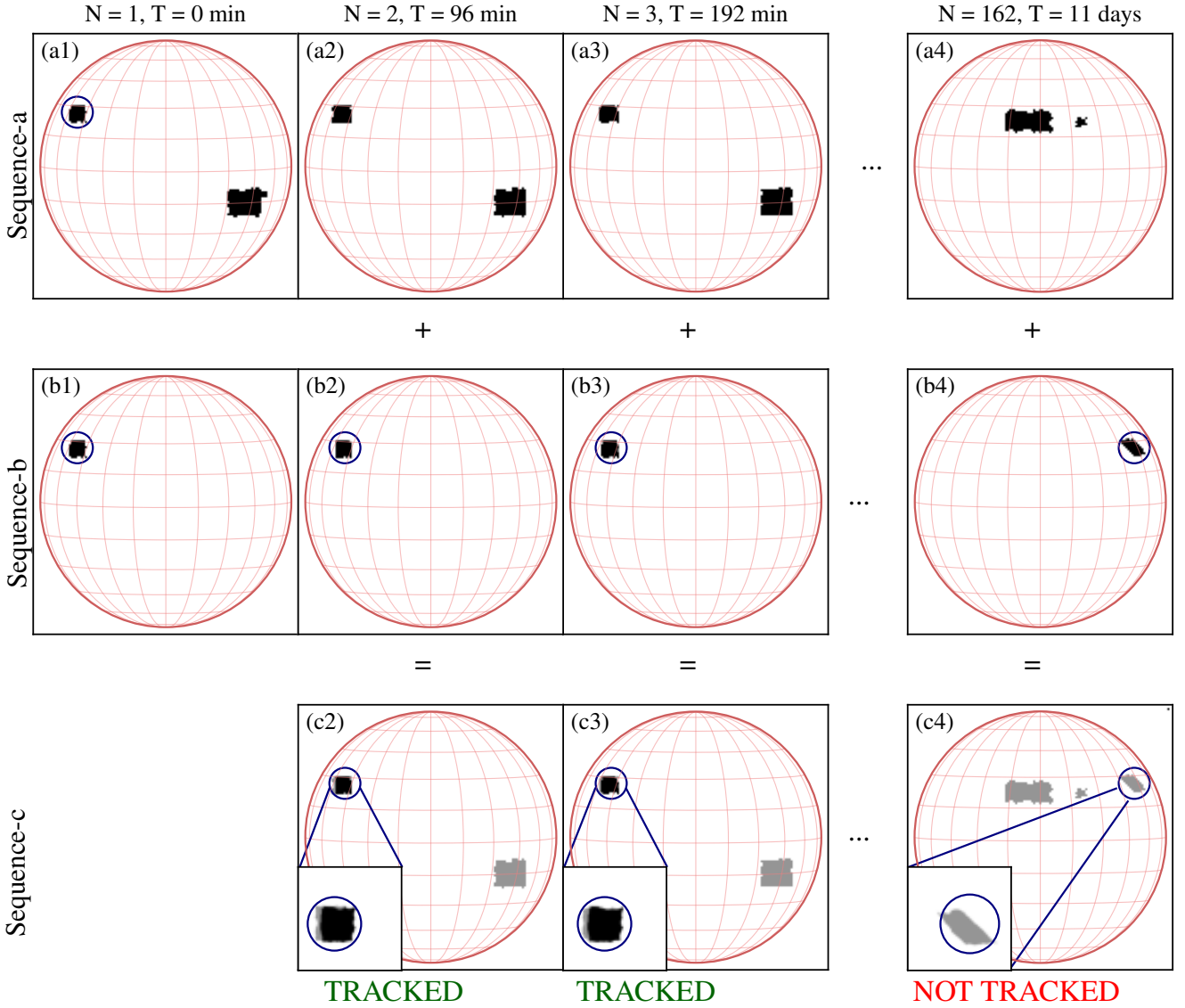[2] We use morph_close.pro function available in IDL for this.

Figure 2: Representative example of the BMR Tracking Algorithm. The BMR intended to be tracked is marked by a circle. (a1), (a2) (a3) and (a4) represents the selected binary maps in Sequence-a. (b1), (b2) (b3) and (b4) represents Sequence-b, the isolated and differenetially rotated binary masks of the BMR, corresponding to the time of observation in Sequence-a. (c2), (c3) and (c4) represents Sequence-c, obtained by adding Sequence-a and Sequence-b. The zoomed in view of overlapping region is shown in inset.

4. The binary mask of isolated BMR (Figure 2b1) is differentially rotated using the drot_map.pro routine in IDL[3], to the time of observation of Sequence-a. For example, b1 is differentially rotated to the time of observation of a2 to obtain b2, similarly, b1 is differentially rotated to the time of a3 to obtain b3, and so on. This is represented by Sequence-b and is shown in Figure 2b1 – b4.

5. In the following step, we add the Sequence-a (Figure 2a1 – a4) with the corresponding differentially rotated binary masks, Sequence-b (Figure 2b1 – b4), e.g., c2=a2+b2, c3=a3+b3 and so on. This is represented by Sequence-c and is shown in Figure 2c2 – c3.

6. Now, we go through all the images in Sequence-c (Figure 2c1 – c3) and check for the overlapping pixels. If the overlap is more than 150 pixels (600 arcsec^2), the BMR is marked as tracked (Figure 2c2 and Figure 2c3), otherwise not tracked

---

[3] It uses differential rotation profile from Howard et al. (1990).

(Figure 2c4). Furthermore, if the overlapping criteria are not met in the consecutive 30 binary masks (i.e. not enough overlap was detected for the next 48 hours), we increase the overlapping criteria to 250 pixels (1000 arcsec^2) for the next observation to ensure that the BMR tracked is the intended one and not a new one.

7. The same BMR-ID i.e., 10001, is assigned to all the tracked BMRs in Sequence-c. At this step, along with BMR-ID, we also store a few other parameters of the tracked BMR.

8. We repeat all the above steps for each BMR present in the selected observation period (Figure 2a1).

9. Once all the BMRs in the first selected observation are tracked, we go for the next observation and track only the new BMRs which are not tracked already. We do this by comparing the BMR-ID with the stored information in the previous step.

3. RESULTS

3.1. *Representative Tracking Results*

To demonstrate the result of our tracking algorithm, in Figure 3, we show the evolution of NOAA region AR9232 (AutoTAB-ID 11436) and AR11390 (AutoTAB-ID 11201), which have been observed in MDI and HMI, respectively. AR9232 was first identified near the East limb (25.2° N, −49.3° E) and has been tracked throughout its disk passage from 18-06-2000 03:11 to 24-06-2000 22:23[4]. Although our algorithm tracks the AR9232 in 113 observations (images), in Figure 3a, we only show one snapshot every day for 7 days. In Figure 3c, we also show the evolution of B_{max} and absolute total flux for AR9232, and we note a systematic and continuous decrease (except small fluctuation) in both these quantities. This continuous decrease suggests that AutoTAB has been able to track the BMR properly, and it has been picked during its decaying phase, which is also inferred from the Figure 3. In contrast with our algorithm, the SMART Algorithm (Higgins et al. 2011) tracks the same region for a shorter period, from 15-11-2000 03:15 to 23-11-2000 20:48.

In Figure 3b, we show the evolution of AR11390 observed in HMI in a similar way as for AR9232. This BMR has been first identified near the East limb (8.3° N, 58.2° E), and AutoTAB tracks it for 8 days (in 122 observations) till it reaches close to the West limb. The

variation of total flux and B_{max} (see Figure 3d) once gain show the continuous and systematic variation over the tracking period. Furthermore, in Figure 3d, we see that the B_{max} as well as absolute total flux, show a small variation initially, and then they start increasing rapidly on day 5. Hence, we infer that this BMR has been tracked from its emergence to the time it crosses the West limb when AutoTAB loses track of it.

Apart from these two BMRs, in Appendix 5, we also show the evolution of another tracked BMR which has been observed in both MDI amd HMI exist (also see Figure 9). The comparison of B_{max} and total flux in these two BMRs confirms that the AutoTAB is working in the same way for both the data sets. Please not that we have scaled up the B_{max} measured in HMI by 1.4 to bring both MDI and HMI at same level (Liu et al. 2012).

By selecting the BMRs randomly from the tracked data, we observe that similar kinds of variations are consistently present in all the tracked BMRs with a few exceptions. Therefore, based on these findings, we say that AutoTAB is very efficient in tracking the BMRs during their appearance on the near side of the Sun. Using our state-of-the-art algorithm, we have tracked 9232 BMRs in Cycle-23 and Cycle-24 for the years 1996 – 2020. In the following section, we will discuss some of the statistical properties of these tracked BMRs.

3.2. *Statistical Properties of BMRs*

In Figure 4, we show the distribution of the lifetime/disk-passage time for all the tracked BMRs. From Figure 4, we note that BMRs exhibit a broad range of lifetimes, varying from several hours to over a week. Although AutoTAB is not able to track a BMR that goes into the far side, it has been tracked only in its evolutionary stage. Other than that, we also encountered a few cases in which the BMR is living for a sufficiently long time, but they have been detected for less than 5% of times, in the number of expected frames[5] due to data gaps, corrupted data, or they have been missed during detection. Hence, after excluding such cases, based on how they were tracked i.e., either for the whole life or only in the evolutionary stage, we classified the BMRs into three classes, which are as follows.

1. **Short Lived (SL):** The BMRs, which emerge and decay in the near side of the Sun and have a lifetime of 8 hours or less, are classified as Short Lived (SL) BMRs. We segregated this class as they mainly comprise small BMRs, which may in-

---

[4] All the mentioned time in this article is in UTC.

[5] Number of expected frames=(Time of last detection-Time of first detection)/cadence of data.
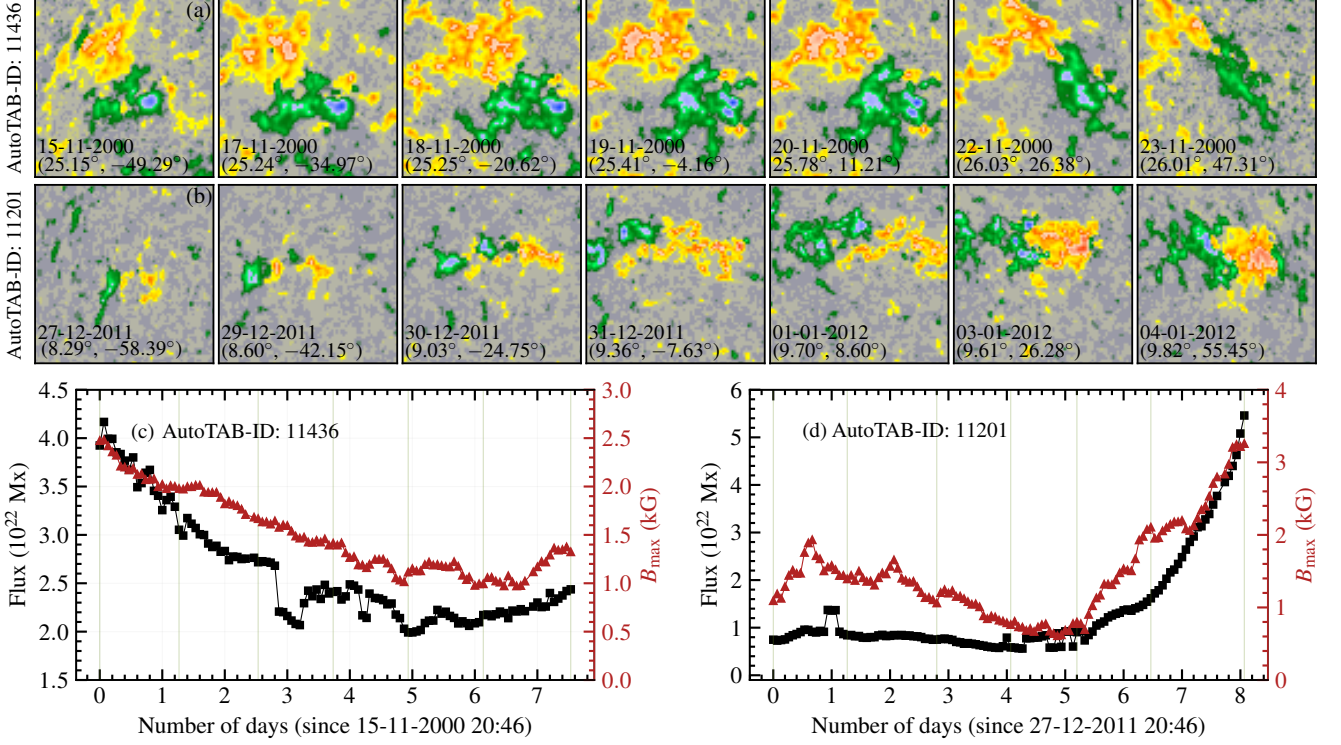
Figure 3: Panels (a) and (b) respectively show the snapshots of the tracked BMRs with AR9232 (AutoTAB-ID 11436) and AR11390 (AutoTAB-ID 11201) corresponding to each day during the tracking. Panels (c) and (d) show the evolution of absolute total flux and B_{max} for these BMRs. The vertical lines in (c) and (d) represent the times corresponding to the time of snapshots shown in (a) and (b), respectively.
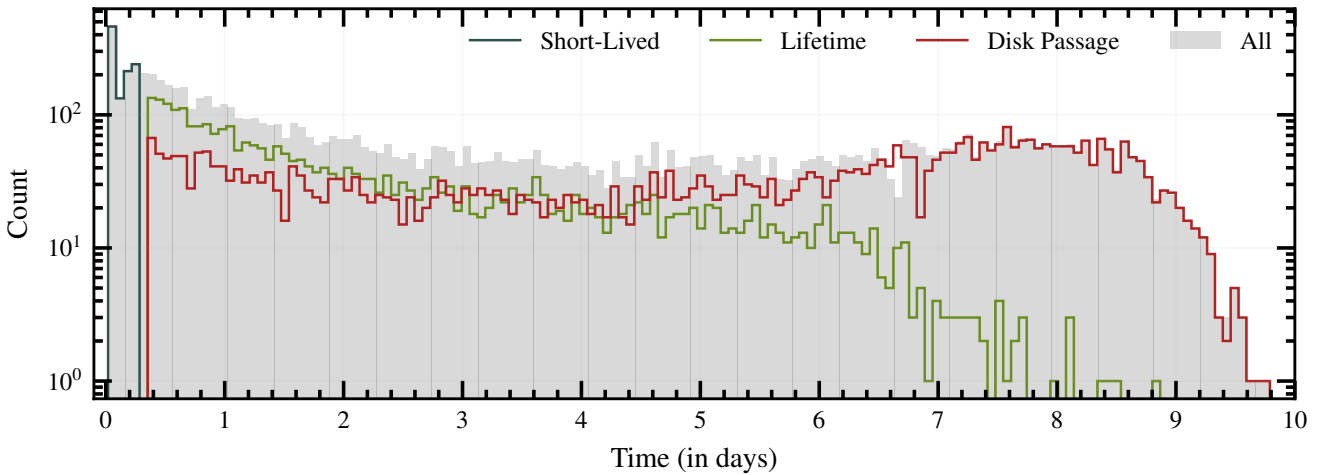

Figure 4: Distribution of the lifetimes of the tracked BMRs of different classes shown by different colors.

clude a few large ephemeral regions with the typical magnetic flux of $\approx 10^{20}$ Mx. The distribution of the SL class appears in the right most of Figure 4. In Figure 5a, we show the evolution of total flux and $B_{\max}$ of a typical BMR (AutoTAB-ID 10076) from this class. It is noted from the Figure 5a that the BMR shown here emerges with relatively low flux and $B_{\max}$ and decays withing a few hours.
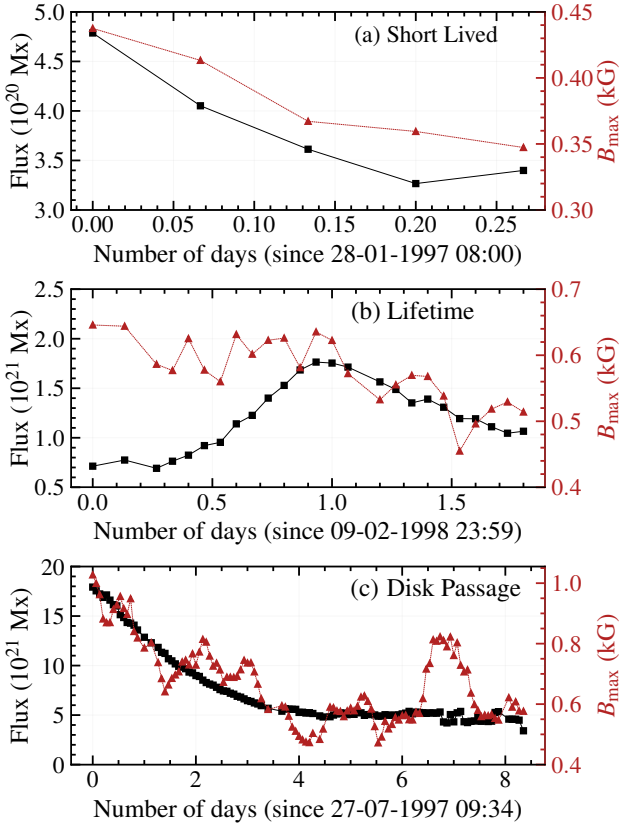
Figure 5: Evolution of absolute total flux and $B_{\max}$ for atypical BMRs from (a) SL, (b)LT and (c)DP classes. AutoTAB-IDs of the BMRs shown in (a), (b), and (c) are 10076, 10213, and 10399, respectively.

2. **Lifetime (LT):** Rest of the tracked BMRs, which have a lifetime of more than 8 hours and have emerged and decayed in the near side of the Sun, i.e., they have been tracked throughout their lifetime, are classified as Lifetime (LT) BMRs. The distribution of the LT class spans around a week (see Figure 4). An example of evolution of such BMR (AutoTAB-ID 10213) is shown in Figure 5b.

3. **Disk Passage (DP):** This class of BMRs has not been tracked for their lifetime. Instead, they have only been tracked for a part of their life span. This class includes all those BMRs, and we classed them as Disk Passage (DP). This class includes (*i*) BMRs that appear near the East limb ($\leq 45°$E) and disappear on the near side, (*ii*) BMRs that appear on the near side of the Sun but cross the West limb (longitude $\geq 45°$ W) and (*iii*) BMRs which appears on the East limb ($\leq 45°$ E) and crosses West limb ($\geq 45°$W). Here we restrict ourselves between the longitudes of $\pm45°$, as the uncertainty in the magnetic field measurement increases towards the limb. Lifetime for this class is distributed all the way from a few hours to more than a week. The evolution of flux and $B_{\max}$ for one such BMR (AutoTAB-ID 10399) is shown in Figure 5c.

The snapshots of the evolution of all the three BMRs in Figure 5 can be found in the data repository[6] for AutoTAB.

The number of BMRs identified in each class is represented in the Table 1 for the period of $1996-2020$. Along with their numbers, we also calculated the mean of area, total flux, $B_{\max}$ and B_{mean} for all these classes, which are listed in Table 1. From this table, we note that all these quantities increases as we go from SL class to LT and DP classes. Hence, we find that the bigger BMRs have longer lifetimes, which is in agreement with the earlier findings from the sunspot (van Driel-Gesztelyi & Green 2015).

After discussing the various classes of BMRs and their time evolutions, we shall now discuss the collective behavior of the BMRs in the aforementioned three classes.

3.2.1. *Solar Cycle Variation*

The first property that we looked for is, does the number of newly emerging BMRs obeys the well-known solar cycle behavior. In contrast to the past studies (e.g., Jha et al. 2020; McClintock & Norton 2016), where the same BMR is counted multiple times during their appearance on the near side, instead here, we only count each tracked BMR once. Therefore, in Figure 6, we show the monthly number of newly emerging BMRs with time for all three classes, SL (Figure 6a), LT (Figure 6b) and DP (Figure 6c). The number of BMRs in LT and DP classes obediently follows the known solar cycle behavior based on the conventional sunspot number. Such behavior is not evident in the case of the SL class. A

Table 1: Some key parameters of different classes of tracked BMRs.

Classification	Number of BMRs	Area $\pm\Delta$Area (μHem)	Flux $\pm\Delta$Flux (10^{22}Mx)	$B_{max}\pm\Delta B_{max}$ (G)	$B_{mean}\pm\Delta B_{mean}$ (G)
Short Lived (SL)	1251	20.17 ± 0.71	0.26 ± 0.01	541.32 ± 5.38	197.46 ± 0.66
Lifetime (LT)	3191	88.65 ± 1.05	1.50 ± 0.02	949.20 ± 6.35	224.46 ± 0.81
Disk Passage (DP)	4710	116.87 ± 0.17	2.05 ± 0.01	1436.83 ± 7.02	281.07 ± 0.71

significant number of SL BMRs are also observed during the solar minima when the toroidal field of the Sun is weak and only a few large BMRs are produced.
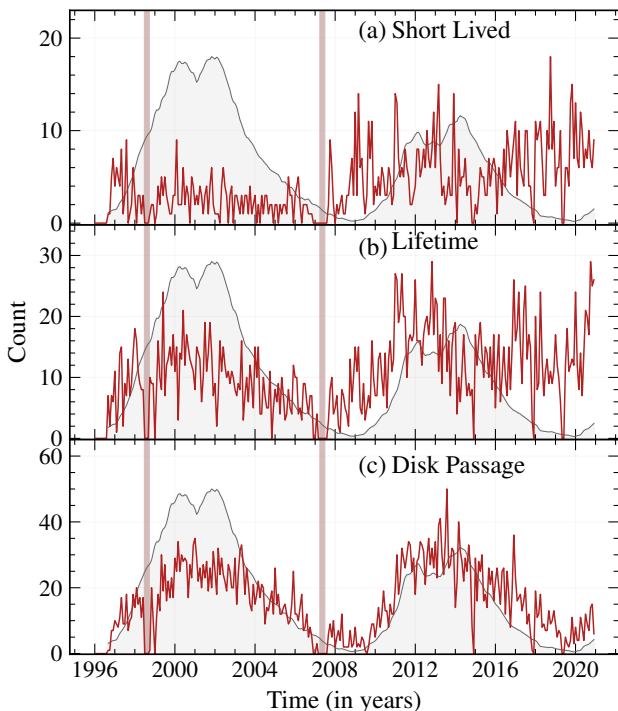
Figure 6: Time series of the monthly number of unique BMRs for (a) SL, (b) LT, and (c) DP classes. The grey-shaded region represent the international smoothed sunspot number (scaled to BMR counts for better representation). Here, vertical strips represent the data gaps.

3.2.2. *Latitude-time Distribution*

Another crucial property of sunspots is their latitudinal distribution (Hathaway 2015; Jha et al. 2022), the so-called 'butterfly diagram'. In Figure 7, we show the time-latitude distribution of identified BMRs for each classes, SL (Figure 7a), LT (Figure 7b) and DP (Figure 7c). Here, each point represents a unique BMR. The latitude and time of all the BMRs are chosen at a time when they attain their maximum total flux (represented by the colors of the points) during the tracking period. We note that for the DP class, the maximum flux may not be the actual maximum flux of the BMR, as AutoTAB only tracked them during a fraction of their life span. The interesting thing to note here is that although the BMR classes LT (Figure 7b) and DP (Figure 7c) follow the well-known butterfly diagram, the SL (Figure 7a) class is more scattered over the latitude (a small latitudinal dependency can still be seen) independent of the phase of the solar cycle. It could be that SL class BMRs that appears from the high latitude at the beginning of the cycle and continues till the end of the cycle at the solar minimum are part of the extended solar cycle (McIntosh et al. 2015). However, Jha et al. (2020) have shown that the two classes of BMRs, namely the BMRs with spot and without spot in white-light images, follow the same latitude-time distribution based on their classification. Further study is required to dig deep into the detail, which will be done in the follow-up paper. Another point to note here is that although the total number of BMRs in Cycle 23 is less than in Cycle 24, the fraction of bigger BMRs that falls in the LT and DP classes is more in Cycle 23.

3.3. *Comparisons with Existing Algorithms*

In this section, we compare our tracking algorithm with the existing BMR tracking algorithms such as SMART (Higgins et al. 2011) and BARD (Muñoz-Jaramillo et al. 2021; Muñoz-Jaramillo et al. 2021, 2016). To compare with SMART, we select four different BMRs tracked by AutoTAB in the year 2008 and compare our findings with SMART's. We have not implemented the SMART algorithm on our data set. Instead, we used Helioviewer (Müller, D. et al. 2017)[7] to get the tracking information about the four selected BMRs (see Table 2).

---

[7] https://helioviewer.ias.u-psud.fr/

Table 2: Tracking details for the four selected BMRs for comparison of AutoTAB with SMART.

NOAA Number	SMART		AutoTAB		
	SMART Id.	Time (dd/mm/2008 hh:mm)	AutoTAB-ID	Time (dd/mm/2008 hh:mm)	Detection
10980	5480.0007	03/01 11:15 − 03/01 19:15	13712	03/01 20:46 − 11/01 07:58	112
	5480.0012	03/01 19:15 − 04/01 01:35			
	.	.			
	.	.			
	5488.0008	11/01 12:47 − 11/01 19:11			
-	5622.0012	24/05 19:15 − 24/0522:27	13768	24/05 19:12 − 25/04 22:24	14
-	5512.0003	04/02 04:51 − 04/02 12:51	13717	03/02 11:22 − 07/02 17:36	40
10999	5646.0005	17/06 08:03 − 17/06 14:27	13776	17/06 15:58 − 25/06 09:36	47
	5646.0009	17/06 14:27 − 17/06 20:47			
	.	.			
	.	.			
	5647.0010	18/06 22:23 − 19/06 04:23			

NOTE—The mentioned times are in UTC. The SMART identifiers and NOAA numbers can be cross-verified at https://helioviewer.ias.u-psud.fr/

The first BMR that we compared is NOAA AR10980, which AutoTAB has successfully tracked for 250 hours from 03-01-2008 20:46 to 11-01-2008 07:58, during its passage across the solar disk with AutoTAB-ID 13712. In contrast, the SMART algorithm tracked the same BMR from 03-01-2008 11:15 to 11-01-2008 19:11 with thirty-one different SMART Identifiers throughout its disk passage. Compared to AutoTAB, SMART started tracking the BMR early in the emergence phase because, in AutoTAB, the detection and tracking are limited to less than 0.9 $R_\odot$.

(ii) The second selected BMR with AutoTAB-ID 13768 does not have an assigned NOAA number (because it is a small BMR and has not appeared as a sunspot). This BMR is relatively small in size and has been identified by SMART for 3 hours. In opposition to SMART, AutoTAB tracked this particular BMR for more than a day throughout its lifetime, which indicates that AutoTAB is doing a better job in tracking of very small features.

(iii) For our third comparison, the BMR we selected with AutoTAB-ID 13717, which also does not have an assigned NOAA number. AutoTAB algorithm tracks this BMR for 102 hours (03-02-2008 11:22 − 07-02-2008 17:36) with 39 detections in between, whereas the SMART algorithm has tracked it for 8 hours with one SMART identifier, which further confirms the efficiency of AutoTAB for smaller BMRs.

(iv) The final BMR that we compare is NOAA 1099 with AutoTAB-ID 13776 on 17-06-2008 and was tracked by the SMART algorithm for two days with 7 different SMART identifiers. For the same BMR, AutoTAB tracked it diligently from 17-06-2008 15:58 to 19-06-2008 09:36 and later with fewer and irregular detections (totaling up to 46 detections) for the next five days. This suggests that tracking the BMRs through the complete disk puts us in an advantageous position, where a BMR can still be tracked even if it has been missed in some observations. Complete details of these four BMRs are shown in Table 2.

Apart from the SMART, we also compared our result with the BARD Tilt catalog (Muñoz-Jaramillo et al. 2016, 2021; Muñoz-Jaramillo et al. 2021) by calculating the monthly new emergence in BARD as well as in AutoTAB algorithm for the overlapping period of 1996-2016, which is represented in the Figure 8. Here, we note that AutoTAB consistently detects more BMRs in both solar cycles, even during the low-activity phase. For Cycle 24, which is weaker than Cycle 23 in terms of sunspot number, AutoTAB detects considerably more BMR than BARD. It could be due to two reasons: (1) HMI data (during cycle 24) comes with less noise, and AutoTAB performs well in it, and (2) more number of small BMRs are observed in Cycle 24 than in Cycle 23 (see Figures 6 and 7). Therefore, it is clear that our automated code AutoTAB can perform well in low-noise magnetogram data. However, during the maximum phase of Cycle 23, AutoTAB possibly misses some BMRs due to the appearance of many close-lying big
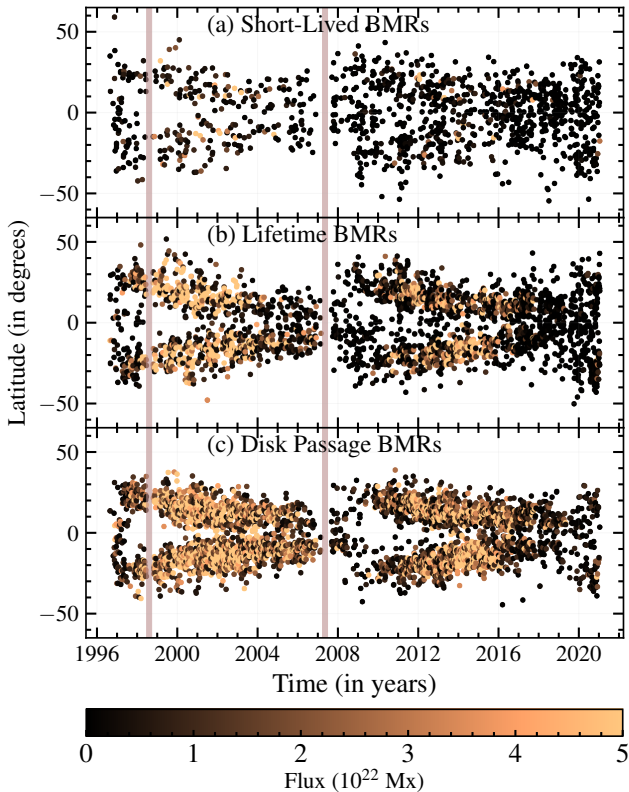
Figure 7: Latitude-time distribution (butterfly diagram) of the tracked BMRs of (a) SL (b) LT, and (c) DP classes. The color of the points represents the total flux of the BMR and the vertical strips represent the data gaps.

BMRs, which are not identified individually in the relatively noisy MDI data.

3.4. *Limitations of Tracking Algorithm*

As with any algorithm, the AutoTAB also has some limitations, which are as follows.

(*i*) One of the biggest challenges that AutoTAB has to face is dealing with the multiple BMRs lying closely together. This issue is mostly carried forward from the detection and also affects the tracking, and occasionally multiple BMRs have been tracked as a single one.

(*ii*) Once BMR crosses the west limb, the AutoTAB loses track of it, but there are a few cases, particularly for long-living BMRs, the same BMR could appear in the East limb after coming back from the far side. In this case, the AutoTAB treats this BMR as a new one and gives the unique AutoTAB-ID to it even though they are the same.

(*iii*) The last but not least, the detection and pre-processing steps are strongly affected by the level of
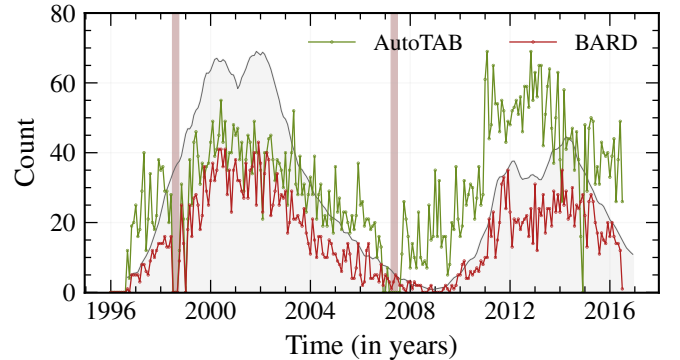
Figure 8: Comparison of the monthly number of newly emergent BMRs obtained from AutoTAB (our) and BARD, along with the traditional monthly sunspot number (grey shaded area enclosed by line). The sunspot number has been multiplied by a factor of 0.6 to bring it to the scale of the BMR count. The vertical strips on the figure represent the data gaps.

noise in the data while identifying the region of interest, and ultimately it also impacts the tracking.

3.5. *Possible Application to Other Data*

So far, we have only discussed and demonstrated the application of AutoTAB on MDI and HMI magnetogram datasets. So the question is, will it be possible for AutoTAB to track the BMRs in other datasets? The answer is yes, but since our algorithm has three major parts (i) detection, (ii) pre-processing, and (iii) tracking, all of them will not work in the same way with different datasets. Although the pre-processing and tracking are expected to work with various datasets, our detection algorithm, which is only optimized for MDI (Stenflo & Kosovichev 2012) and HMI (Jha et al. 2020) magnetograms, may not work with other data sets. Thus, for a given binary mask of the region of interest, the tracking algorithm can be used, along with pre-processing technique. Here, we would like to emphasize that even for pre-processing and tracking, a few constants or thresholds, such as morph closing kernel size, overlapping area threshold, etc., need to be tuned according to the data. Furthermore, the AutoTAB tracking algorithm can also be used to track the other features in the solar atmosphere by optimizing these parameters.

4. CONCLUSIONS

Observational study of the evolving properties of BMRs is crucial to understand the origin of solar magnetic field and cycle. However, due to the unavailability of a completely automatic and efficient BMR tracking algorithm, the study of the temporal evolutions of

various properties of BMRs is limited. We have developed an automatic algorithm, AutoTAB for tracking the BMR from magnetograms. It works by taking the binary maps of the detected BMR as inputs. For detecting BMRs from magnetograms, we also build an algorithm following the idea of Stenflo & Kosovichev (2012) and Jha et al. (2020). Using our developed detection algorithm, we have produced the binary maps of the detected BMRs from HMI and MDI during the solar cycles 23 and 24. By feeding these binary maps in AutoTAB, we have produced a homogeneous and comprehensive data set for 9152 tracked BMRs.

AutoTAB is successful in tracking the identified BMRs through their life on the visible solar disk and in capturing their evolving magnetic and morphological properties. Representative examples of the dataset have been presented by showing the snapshots of the evolution of the BMRs at various stages of their life along with the progression of unsigned flux and B_{max}. Further, case studies have been performed on the method's efficiency with other existing tracking methods. The study indicates that AutoTAB successfully tracks the BMRs inside the 0.9 $\mathrm{R}_\odot$ with better accuracy and consistency than the SMART. As AutoTAB works by checking for the overlap between consecutive binary maps, it remains independent of the dataset used and can work efficiently for tracking other solar features. A comparison between the number of new emergent BMRs in AutoTAB and the BARD catalog shows that AutoTAB consistently detects and tracks more BMRs through the past two solar cycles compared to BARD. As AutoTAB is fully automatic, multiple closely lying BMRs might have been identified as one, which remains one of the major challenges faced by AutoTAB which needs to be addressed in the future.

AutoTAB tracks the BMR in a wide range of its lifetime, from hours to days, which leaves us with a large volume of tracked information. Hence, the tracked BMRs have been classified into different groups, namely, Short Lived (lives for less than 8 hours), Lifetime (emerges and disperses in the visible surface), and Disk Passage (coming/going from/to the farside of the Sun). The tracked BMRs show the usual signatures of solar cycle variation. We also observe that the Lifetime and Disk Passage BMRs follow familiar latitudinal and temporal distributions as seen by the sunspot butterfly diagram. This distribution is not observed in the case of Short Lived BMRs as they are the small features that appear at all times on the Sun. In a follow-up publication, we shall further exploit the results of tracked BMRs to compute various properties of BMR which will help us to identify the origin of BMR formation.

5. APPENDIX: COMPARISON OF THE TRACKING RESULTS FROM MDI AND HMI MAGNETOGRAMS

Figure 9a and Figure 9b show the evolution of NOAA AR11068 from HMI and MDI, respectively. AutoTAB tracked this particular BMR for a total duration of 153 hours from 05-05-2010 19:10 to 12-05-2010 04:46, during its passage across the solar disk, with AutoTAB-ID 10349. As this BMR has been identified in the period when we have observation from both the instruments (HMI and MDI). Hence, we track it in both the data sets for comaparision. Though this BMR was tracked for the same period of time in both datasets, AutoTAB could track it more consistently with HMI data (97 detections) compared to MDI, with only 87 detections. Less detection in MDI is expected because of relatively larger noise in the data as compared to HMI data. Nevertheless, upon closer examination of the evolution of total flux and Bmax throughout the lifespan of BMR (as shown in Figure 9c and Figure 9d), we observe that the B_{max} and absolute total flux show outstanding agreement in both the data sets. For this particular BMR, the total flux consistently decreases over the lifetime of the BMR, while B_{max} show a small increase in the first few hours and subsequently decreases. This small increase could be due to the uncertainity in the measurment of B_{max} near the limb.
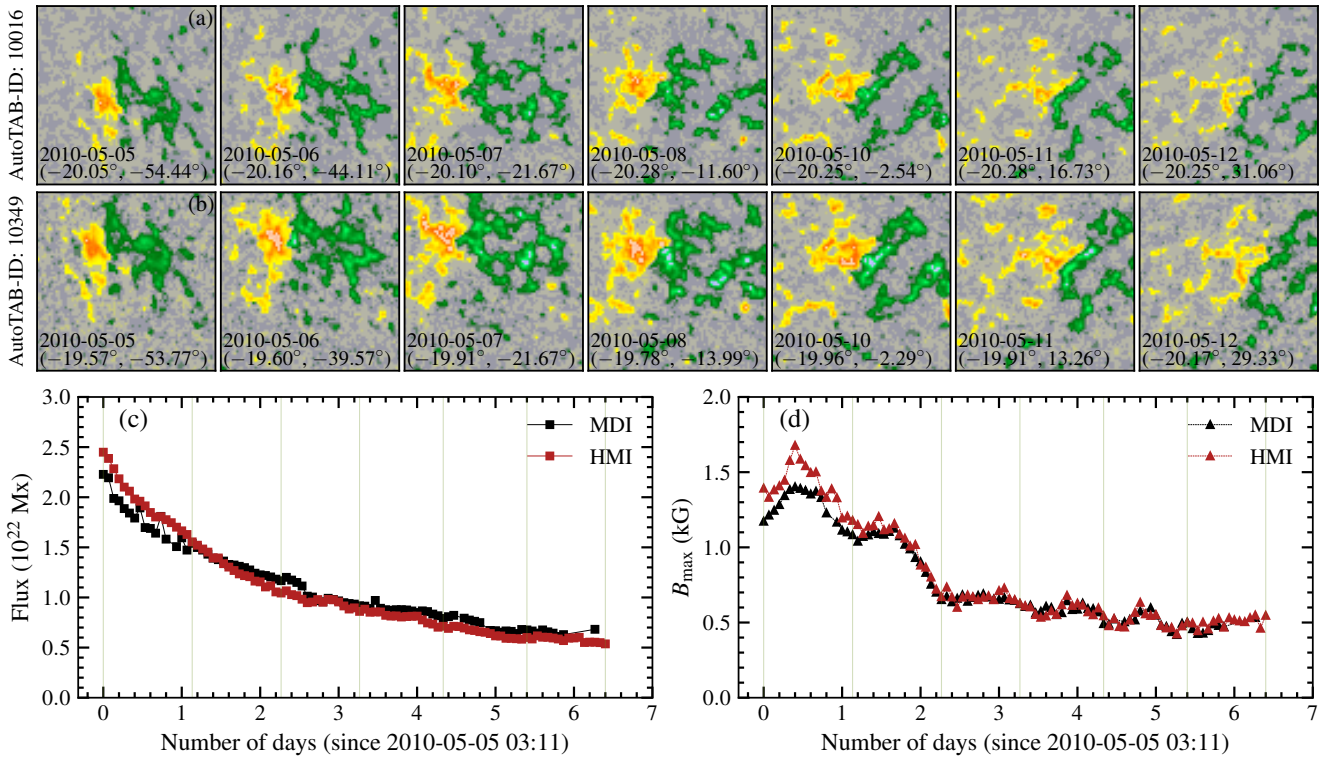
Figure 9: Snapshot of tracked BMR (NOAA AR11068) during its passage on the observable disk as observed in (a) HMI and (b) MDI. Panels (c) and (d) show the variations of the total flux and $B_{\max}$ respectively, as observed in both the data sets. The vertical lines in (c) and (d) represent the times corresponding to the snapshots shown in (a) and (b), respectively.

REFERENCES

Babcock, H. W. 1961, ApJ, 133, 572, doi: 10.1086/147060

Bobra, M. G., Sun, X., Hoeksema, J. T., et al. 2014, SoPh, 289, 3549, doi: 10.1007/s11207-014-0529-3

Bobra, M. G., Wright, P. J., Sun, X., & Turmon, M. J. 2021, The Astrophysical Journal Supplement Series, 256, 26, doi: 10.3847/1538-4365/ac1f1d

Dasi-Espuig, M., Solanki, S. K., Krivova, N. A., Cameron, R., & Peñuela, T. 2010, A&A, 518, A7, doi: 10.1051/0004-6361/201014301

Getling, A. V., & Buchnev, A. A. 2019, ApJ, 871, 224, doi: 10.3847/1538-4357/aafad9

Hale, G. E., Ellerman, F., Nicholson, S. B., & Joy, A. H. 1919, ApJ, 49, 153, doi: 10.1086/142452

Harvey, J. W., Hill, F., Hubbard, R. P., et al. 1996, Science, 272, 1284, doi: 10.1126/science.272.5266.1284

Hathaway, D. 2015, Living Rev. Sol. Phys., 39, 227, doi: 10.1007/lrsp-2015-4

Higgins, P. A., Gallagher, P. T., McAteer, R. T. J., & Bloomfield, D. S. 2011, Advances in Space Research, 47, 2105, doi: 10.1016/j.asr.2010.06.024

Howard, R. F. 1991, SoPh, 136, 251, doi: 10.1007/BF00146534

—. 1996, SoPh, 169, 293, doi: 10.1007/BF00190606

Howard, R. F., Harvey, J. W., & Forgach, S. 1990, SoPh, 130, 295, doi: doi:10.1007/bf00156795

Jha, B. K., Hegde, M., Priyadarshi, A., et al. 2022, Frontiers in Astronomy and Space Sciences, 9, 1019751, doi: 10.3389/fspas.2022.1019751

Jha, B. K., Karak, B. B., Mandal, S., & Banerjee, D. 2020, ApJL, 889, L19, doi: 10.3847/2041-8213/ab665c

Jha, B. K., Priyadarshi, A., Mandal, S., Chatterjee, S., & Banerjee, D. 2021, SoPh, 296, 25, doi: 10.1007/s11207-021-01767-8

Keller, C. U., Harvey, J. W., & Giampapa, M. S. 2003, in Innovative Telescopes and Instrumentation for Solar Astrophysics, ed. S. L. Keil & S. V. Avakyan, Vol. 4853, International Society for Optics and Photonics (SPIE), 194 – 204, doi: 10.1117/12.460373

LaBonte, B. J., Georgoulis, M. K., & Rust, D. M. 2007, ApJ, 671, 955, doi: 10.1086/522682

Leighton, R. B. 1964, ApJ, 140, 1547, doi: 10.1086/148058

Liu, Y., Hoeksema, J. T., Scherrer, P. H., et al. 2012, SoPh, 279, 295, doi: 10.1007/s11207-012-9976-x

McAteer, R. T. J., Gallagher, P. T., Ireland, J., & Young, C. A. 2005, SoPh, 228, 55, doi: 10.1007/s11207-005-4075-x

McClintock, B. H., & Norton, A. A. 2016, ApJ, 818, 7, doi: 10.3847/0004-637X/818/1/7

McIntosh, S. W., Leamon, R. J., Krista, L. D., et al. 2015, Nature Communications, 6, 6491, doi: 10.1038/ncomms7491

Mordvinov, A. V., Karak, B. B., Banerjee, D., et al. 2022, MNRAS, 510, 1331, doi: 10.1093/mnras/stab3528

Muñoz-Jaramillo, A., Navarrete, B., & Campusano, L. E. 2021, ApJ, 920, 31, doi: 10.3847/1538-4357/ac133b

Muñoz-Jaramillo, A., Werginz, Z., Vargas-Acosta, J. P., et al. 2016, in 2016 IEEE International Conference on Big Data (Big Data, 3194–3203, doi: 10.1109/BigData.2016.7840975

Müller, D., Nicula, B., Felix, S., et al. 2017, A&A, 606, A10, doi: 10.1051/0004-6361/201730893

Muñoz-Jaramillo, A., Werginz, Z., Vargas, J. P., DeLuca, M., & Navarrete, B. 2021, Bipolar Active Regions Detection (BARD) Tilt Catalog, V3, Harvard Dataverse, doi: 10.7910/DVN/QEMSZ2

Scherrer, P. H., Bogart, R. S., Bush, R. I., et al. 1995, SoPh, 162, 129, doi: 10.1007/BF00733429

Schou, J., Scherrer, P. H., Bush, R. I., et al. 2012, SoPh, 275, 229, doi: 10.1007/s11207-011-9842-2

Schrijver, C. J. 2009, Advances in Space Research, 43, 739, doi: 10.1016/j.asr.2008.11.004

Schunker, H., Baumgartner, C., Birch, A. C., et al. 2020, A&A, 640, A116, doi: 10.1051/0004-6361/201937322

Schunker, H., Birch, A. C., Cameron, R. H., et al. 2019, A&A, 625, A53, doi: 10.1051/0004-6361/201834627

Schwabe, H. 1844, Astronomische Nachrichten, 21, 233, doi: 10.1002/asna.18440211505

Sivaraman, K. R., Gokhale, M. H., Sivaraman, H., Gupta, S. S., & Howard, R. F. 2007, ApJ, 657, 592, doi: 10.1086/510546

Stenflo, J. O., & Kosovichev, A. G. 2012, ApJ, 745, 129, doi: 10.1088/0004-637X/745/2/129

Tlatov, A. G., & Pevtsov, A. A. 2014, SoPh, 289, 1143, doi: 10.1007/s11207-013-0382-9

Ugarte-Urra, I., Upton, L., Warren, H. P., & Hathaway, D. H. 2015, ApJ, 815, 90, doi: 10.1088/0004-637X/815/2/90

van Driel-Gesztelyi, L., & Green, L. M. 2015, Living Reviews in Solar Physics, 12, 1, doi: 10.1007/lrsp-2015-1